

# Single Particle Reconstructions of the Transferrin–Transferrin Receptor Complex Obtained with Different Specimen Preparation Techniques

Yifan Cheng<sup>1</sup>, Elmar Wolf<sup>1</sup>, Mykol Larvie<sup>2</sup>, Olga Zak<sup>3</sup>, Philip Aisen<sup>3</sup>  
Nikolaus Grigorieff<sup>4</sup>, Stephen C. Harrison<sup>2</sup> and Thomas Walz<sup>1\*</sup>

<sup>1</sup>Department of Cell Biology  
Harvard Medical School, 240  
Longwood Avenue, Boston  
MA 02115, USA

<sup>2</sup>Howard Hughes Medical  
Institute, Children's Hospital  
and Department of Biological  
Chemistry and Molecular  
Pharmacology, Harvard  
Medical School, 320 Longwood  
Avenue, Boston, MA 02115  
USA

<sup>3</sup>Department of Physiology  
and Biophysics, Albert Einstein  
College of Medicine, 1300  
Morris Park Avenue, Bronx  
NY 10461, USA

<sup>4</sup>Howard Hughes Medical  
Institute, Rosenstiel Basic  
Medical Sciences Research  
Center, Department of Bio-  
chemistry, Brandeis University  
415 South Street, Waltham  
MA 02454, USA

The outcome of three-dimensional (3D) reconstructions in single particle electron microscopy (EM) depends on a number of parameters. We have used the well-characterized structure of the transferrin (Tf)–transferrin receptor (TfR) complex to study how specimen preparation techniques influence the outcome of single particle EM reconstructions. The Tf–TfR complex is small (290 kDa) and of low symmetry (2-fold). Angular reconstitution from images of vitrified specimens does not reliably converge on the correct structure. Random conical tilt reconstructions from negatively stained specimens are reliable, but show variable degrees of artifacts depending on the negative staining protocol. Alignment of class averages from vitrified specimens to a 3D negative stain reference model using FREALIGN largely eliminated artifacts in the resulting 3D maps, but not completely. Our results stress the need for critical evaluation of structures determined by single particle EM.

© 2005 Elsevier Ltd. All rights reserved.

\*Corresponding author

**Keywords:** transferrin receptor–transferrin complex; specimen preparation; angular reconstitution; random conical tilt; cryo-negative staining

## Introduction

Single particle electron microscopy (EM) has become a standard approach for determining the three-dimensional (3D) structure of biological molecules at intermediate resolution (20–7 Å). Single particle EM has contributed to elucidating structures of large macromolecular complexes

several MDa in size, such as viruses,<sup>1,2</sup> the ribosome<sup>3,4</sup> and the spliceosome,<sup>5,6</sup> as well as to determining structures of molecules as small as a few hundred kDa, such as the spliceosomal U1 small nuclear ribonucleoprotein particle,<sup>7</sup>  $\alpha$ -latrotoxin oligomers,<sup>8</sup> and the transferrin (Tf)–transferrin receptor (TfR) complex.<sup>9</sup> A problem in single particle EM is that it is often difficult to decide whether a 3D reconstruction is correct, if no other structural information is available. The quality and thus the reliability of a 3D reconstruction are often judged on the basis of two criteria. First, a plot of the angular distribution of the particle images reveals whether the data set contains all the views that are

Abbreviations used: Tf, transferrin; TfR, transferrin receptor; EM, electron microscopy; CTF, contrast transfer function; SNR, signal-to-noise.

E-mail address of the corresponding author:  
[twalz@hms.harvard.edu](mailto:twalz@hms.harvard.edu)

necessary to completely define the structure. Second, comparison of projections from the reconstructed 3D map with the class averages or the raw particle images can verify that the 3D structure is consistent with the projection data. The presence of all required views thus validates that the structure of the molecule is completely defined, whereas a good match between the density map and the projection data confirms that the 3D reconstruction is consistent with the raw data. While it is essential to assess a 3D reconstruction by both of these criteria, neither one addresses the question of whether the final reconstruction is indeed a correct representation of the imaged molecule. It is therefore important to understand the factors that influence and possibly distort the outcome of a 3D reconstruction. Here, we have undertaken an array of experiments to study the influence of the specimen preparation technique on the quality of the single particle reconstructions that can be obtained.

Two approaches are currently used in single particle EM, as opposed to electron tomography, to calculate a 3D reconstruction from projection images: random conical tilt<sup>10</sup> and angular reconstitution.<sup>11</sup> In the random conical tilt method, the specimen is imaged twice, first at a high tilt angle and then untilted. The particles from the images of the untilted specimen are translationally and rotationally aligned to each other to determine the  $x$ ,  $y$  coordinates of the center and the in-plane rotations of all the particles. Together with the tilt angle chosen for imaging the specimen, all the orientational parameters needed to reconstruct a 3D map are thus unambiguously defined. For this approach to be practical, the specimen should adsorb to the carbon support in one or only a few orientations. This is often the case for negatively stained specimens where the particles are embedded in a layer of heavy-metal salts.<sup>12</sup> Preferred orientations are particularly beneficial when working with heterogeneous specimens, as they allow separation of particles in different conformations by classification (recently illustrated<sup>13</sup>). The random conical tilt 3D reconstruction approach applied to images of negatively stained specimens thus allows one to calculate 3D reconstructions of molecules in different conformations from images of the same EM grid. Negative staining is known, however, to introduce specimen preparation artifacts. For example, incomplete stain embedding renders invisible the part of the protein that protrudes from the stain layer and drying of the grid usually results in flattening of the specimen.

By contrast, vitrification, the embedding of a sample in a thin layer of vitrified ice,<sup>14</sup> introduces virtually no artifacts and is considered the best specimen preparation technique. Furthermore, unlike negative staining, sample vitrification does not limit the resolution that can be achieved. Vitrified particles usually adopt more or less randomly distributed orientations in the amorphous ice layer, which can be exploited

to calculate an initial 3D reconstruction using the angular reconstitution approach. Five parameters, the  $x$ ,  $y$  coordinates of the center and the three Euler angles, have to be determined for each particle to calculate an initial density map. Euler angles for the particles are determined using the common-lines method.<sup>15</sup> The contrast of images taken from vitrified specimens is very low, because of the small difference in electron scattering between the vitrified ice layer and the embedded molecules. Therefore, the particles are first grouped into an appropriate number of classes to produce averages with an improved signal-to-noise ratio (SNR). These are then used for Euler angle assignment. Angular reconstitution using images of vitrified specimens suffers from two problems. First, vitrification is often not suitable for heterogeneous specimens, because it is not always possible to decide whether two dissimilar images are indeed images of two different particles, e.g. particles in different conformations, or are images of the same particle but in different orientations. Second, angular reconstitution attempts to solve a problem that under unfavorable conditions can have more than one solution. A 3D structure will always produce the same set of projection images, but if certain important views are missing, leaving the 3D structure partially undefined, a set of projection images can produce different 3D reconstructions that are all consistent with the projection data. Once an initial model has been produced, by either method, the 3D reconstruction is improved by refinement of the orientational parameters of the particle images. Although different strategies have been implemented in different program packages, e.g. IMAGIC,<sup>16</sup> SPIDER,<sup>17</sup> EMAN,<sup>18</sup> and FREALIGN,<sup>19</sup> they all rely on iterative cycles of refining the alignment of the projection images to a reference 3D model.

We have previously used single particle cryo-electron microscopy to determine the structure of the human Tf–TRf complex, a 2-fold symmetric complex with a molecular mass of 290 kDa, to a nominal resolution of 7.5 Å.<sup>9</sup> By docking the crystal structures of Tf and TRf into the density map, we could build an atomic model for this complex. In the work reported here, we have used the structurally well characterized Tf–TfR complex to systematically assess the influence of the specimen preparation technique on the outcome of a 3D reconstruction obtained by single particle electron microscopy.

## Results

### Vitrified Tf–TfR complex

Recombinant human Tf–TfR complex was applied to holey carbon film, blotted with filter paper and vitrified by plunging into liquid ethane. Individual complexes could clearly be identified in low-dose images of such preparations (Figure 1(a)),

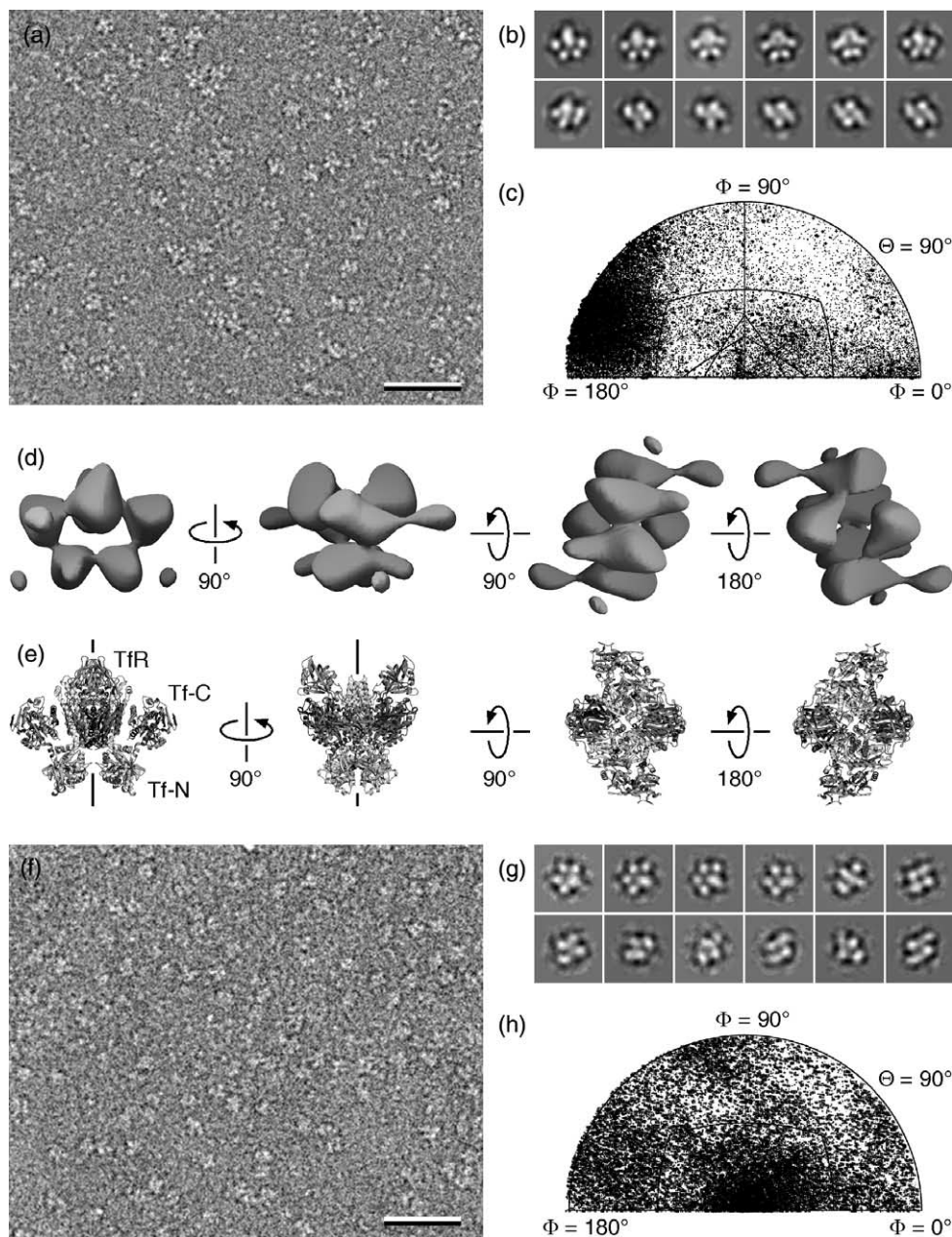


**Figure 1.** Vitrified Tf-TfR complex. (a) Low-dose image of vitrified Tf-TfR complexes prepared using holey carbon film. (b) Gallery of representative class averages displaying various views of the Tf-TfR complex. (c) Plot of the Euler angle distribution showing that the complex has a tendency to adopt preferred orientations in the vitrified ice layer. (d) Views of the best initial 3D reconstruction obtained by the angular reconstitution approach implemented in the IMAGIC software. (e) The same views as in (d) for the atomic model of the Tf-TfR complex. The lines in the first two panels indicate the 2-fold axis. (f) Low-dose image of Tf-TfR complexes vitrified on a continuous carbon film. (g) Gallery of representative class averages revealing that Tf-TfR complexes vitrified on a continuous carbon film do not adopt preferred orientations. (h) Plot of the Euler angle distribution showing that the particles adsorb to the carbon film in random and almost completely uniformly distributed orientations. The scale bars in (a) and (f) represent 50 nm and the individual panels in (b) and (g) have a side length of 27 nm.

and we interactively selected about 36,000 particles for digital image processing. We used the IMAGIC software package<sup>16</sup> to classify the particle images into 500 classes by several cycles of multi-reference alignment (MRA) and multi-variance statistical analysis (MSA) followed by classification (Figure 1(b)). When we used the angular reconstitution algorithm implemented in IMAGIC to generate an initial model (see Materials and Methods for

details), we found that different attempts resulted in very different density maps. The 3D maps depended not only on the class averages we selected, but also on the order in which we introduced them into the reconstruction procedure. This problem has been recognized before and was addressed by an algorithm that simultaneously determines the orientations for a set of projections.<sup>20</sup> However, this alternative approach did not completely resolve

the problem, as the density maps still depended on the number and sets of projection averages that were included in the reconstruction (data not shown). We would therefore not have been able to decide which density map to choose for further structural refinement if no additional structural information had been available. Because the crystal structures of Tf<sup>21</sup> and TfR<sup>22</sup> were available, we were able to identify the 3D map produced by angular reconstitution that was most consistent with these crystal structures, although even this map (Figure 1(d)) looked only remotely similar to the final atomic model we produced for the Tf–TfR complex<sup>9</sup> (Figure 1(e)). Using FREALIGN<sup>19</sup> to refine the orientational parameters of the particles against this initial model, we obtained the previously published density map at a nominal resolution of 7.5 Å.<sup>9</sup> A plot of the Euler angles showed that views were distributed more or less across the entire orientational space, although there was a clear preference for some of the particle orientations (Figure 1(c)).

We were concerned by the different initial models produced by the angular reconstitution approaches. We hoped to overcome this problem by calculating a 3D reconstruction using random conical tilt, because here the orientational parameters of the particles are uniquely defined. For this approach to be practical, the particles should display preferred views. Therefore, in an attempt to induce preferred orientations, we vitrified Tf–TfR complexes that had been adsorbed to a continuous carbon film. Low-dose images taken from such preparations looked very similar to those taken from samples on holey carbon film, although the image contrast was slightly weaker due to the noise introduced by the carbon support (Figure 1(f)). We interactively selected 21,719 particles and classified them into 200 classes. The resulting class averages showed many different views of the Tf–TfR complex, demonstrating that adsorption to continuous carbon film did not introduce preferred orientations of the complexes (Figure 1(g)). Since this preparation was not suitable for obtaining a 3D reconstruction by random conical tilt, we used FREALIGN to align the particle images to our previously determined 3D map of the Tf–TfR complex. A plot of the Euler angles (Figure 1(h)) revealed that the orientations adopted by complexes vitrified on a continuous carbon film were also random and even more uniformly distributed than those of complexes vitrified in holes of holey carbon film (Figure 1(c)).

We finally collected tilt pairs of vitrified Tf–TfR complexes in holey carbon film, assuming that if we collected a large number of images, a suitable number of the molecules would be in a particular orientation. We found, however, that the Tf–TfR complex is too small to be clearly seen in images of tilted specimens due to the thicker ice layer (data not shown), making it impossible to determine the structure of the vitrified Tf–TfR complex by random conical tilt.

## Negatively stained Tf–TfR complex

Vitrification of Tf–TfR complex using holey or continuous carbon film did not show clear preferred orientations and was therefore not suitable for calculating 3D reconstructions by random conical tilt. Previous EM experiments showed, however, that preferred adsorption of the Tf–TfR complex to the carbon support could be induced by negative staining.<sup>13</sup>

### Conventional negative staining with uranyl formate

A Tf–TfR complex sample was adsorbed to a glow-discharged carbon film and negatively stained with uranyl formate as described before.<sup>13</sup> The specimen was imaged at tilt angles of 60° and 0° (Figure 2(a) and (b)). Since in the conventional negative staining technique the particles are not embedded in a continuous layer of stain, images of 60° tilted samples show dark shadows below the molecules resulting from stain accumulation (stain clouds) surrounding individual particles (Figure 2(b)). We interactively selected 8410 pairs of particles from 80 image pairs using the display program WEB associated with the SPIDER software package.<sup>17</sup> Classification calculations showed that most of the particles from images of the untilted sample fell into two classes. A majority of the particles adsorbed to the grid presented a side view (Figure 2(c), panel 1), while most of the remaining particles presented a top view (Figure 2(c), panel 2).

We combined the images of all classes that showed the same view of the complex and a crisp fine structure, and we used the combined particles from the images of the tilted sample to calculate 3D reconstructions. We first calculated a 3D map of the particles presenting the side view (Figure 2(c), panel 1). The unsymmetrized map clearly resolved a density representing the TfR as well as densities representing both the N and the C-lobe of the two bound Tf molecules (Figure 2(d)). The map also revealed distortions. The first view of the reconstruction shows that one of the Tf C-lobes (marked by an asterisk in Figure 2(d)) is clearly smaller than the other C-lobe and the two N-lobes. Furthermore, the third and fourth views of the reconstruction show the left side of the complex to be flat. This flat surface most likely reflects a deformation of the complex resulting from its interaction with the carbon film. Since the Tf–TfR complex is 2-fold symmetric, we applied this symmetry to the reconstruction and then fit the TfR and Tf crystal structures into the resulting density map (Figure 2(e)). The 2-fold symmetrization of the map removed the distortions mentioned above, rendering all four Tf lobes of equal size and eliminating the flat surface where the molecule interacts with the carbon film. The fit of crystal structures showed, however, that the density for the TfR was still substantially deformed. Rather than revealing the characteristic butterfly shape of the TfR dimer, the second view of the symmetrized

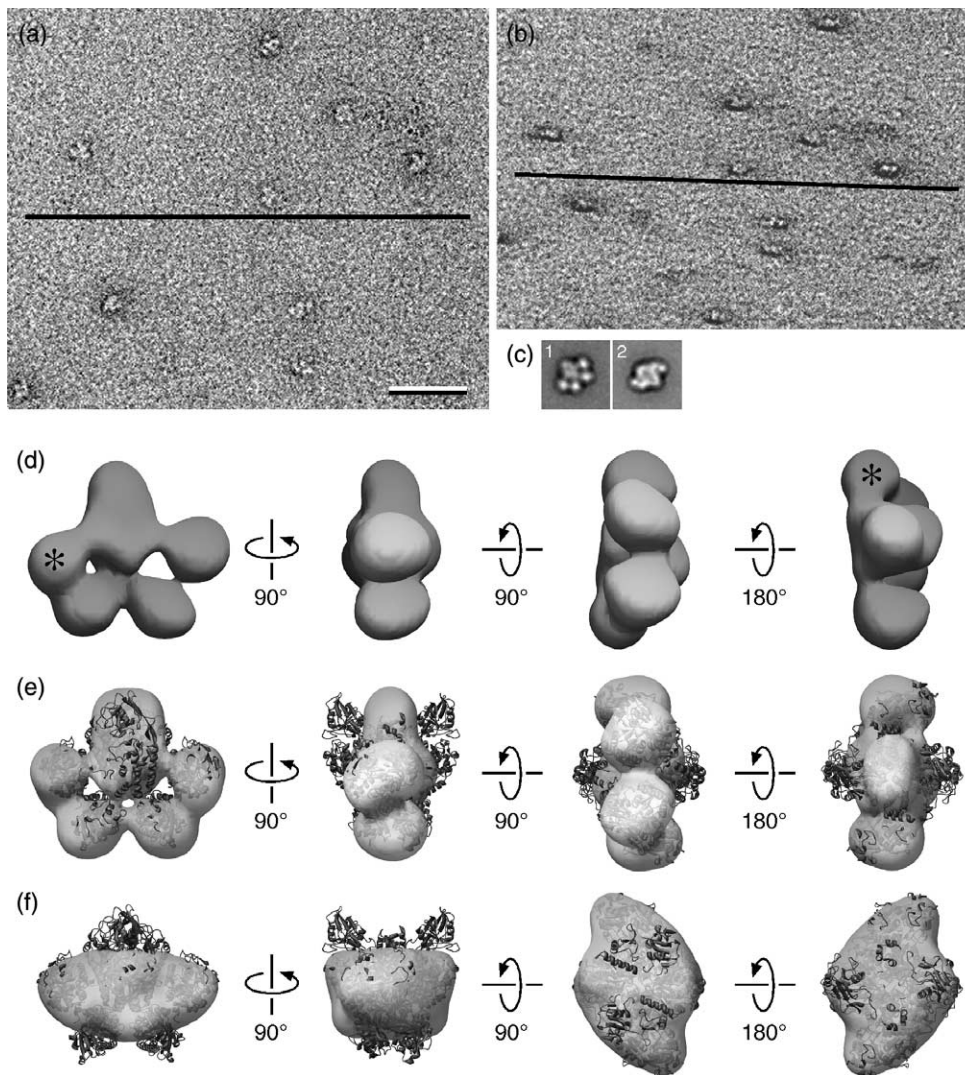


**Figure 2.** Tf-TfR complex prepared by conventional negative staining. (a) and (b) Low-dose images of negatively stained preparations recorded at tilt angles of (a)  $0^\circ$  and (b)  $60^\circ$ . The image of the tilted specimen shows the characteristic shadows below the particles. (c) Class averages showing the two preferred orientations in which the Tf-TfR complex adsorbs to the carbon film; panel 1, side view; panel 2, top view. (d) Views of the unsymmetrized random conical tilt reconstruction obtained with the side view particles (class 1 in (c)) showing a smaller density for one of the Tf C-lobes and loss of the characteristic butterfly shape of the receptor. (e) Same density map as in (d) after 2-fold symmetrization. Fitting of the Tf and TfR crystal structures into the density map reveals that the 3D reconstruction is flattened, particularly the density representing the TfR. (f) 2-fold symmetrized 3D reconstruction using the top view particles (class 2 in (c)) revealing substantial flattening and a lack of distinct structural features. The scale bar in (a) represents 50 nm and the individual panels in (c) have a side length of 27 nm.

reconstruction in Figure 2(e) shows a featureless density with no indication of the bipartite organization of the TfR dimer. The density for the TfR is also severely affected by flattening. Rather than the width of 13.7 nm in the crystal structure, the density map representing the TfR has a width of only 7.5 nm, a flattening of about 45%.

We also calculated a 3D reconstruction using the particles that had adsorbed to the grid presenting a top view (Figure 2(c), panel 2). While flattening mostly affects the density representing TfR in maps reconstructed from “side view particles” (Figure 2(e)), it affects the entire complex in the 3D reconstruction of “top view particles” (Figure 2(f)). As seen in the first two views of the reconstruction in

Figure 2(f), the atomic model protrudes from the 3D map due to a substantial flattening of  $\sim 55\%$ . Probably because of this flattening, the unsymmetrized map (not shown) as well as the 2-fold symmetrized map (Figure 2(f)) show very few features of the Tf-TfR complex. All the densities in the symmetrized map are fused, resolving neither the separation between TfR and Tf nor the cleft between the Tf N and C-lobes.

#### *Negative staining with uranyl formate using a carbon film sandwich*

Incomplete stain embedding renders invisible any protein domains protruding from the stain

layer. Since the images taken from the 60° tilted samples showed prominent stain clouds (Figure 2(b)), incomplete stain embedding provided a potential explanation for the flattening seen in the 3D reconstructions (Figure 2(d)–(f)). To address this problem, we employed the carbon sandwich technique, previously used to visualize, for example, the ribosome.<sup>23</sup> The Tf–TfR complex was adsorbed to a single layer of carbon film and negatively stained with uranyl formate. Another layer of carbon film was then deposited on the specimen, so that the Tf–TfR complexes were now sandwiched between two layers of carbon and embedded in a continuous layer of stain. The details of this procedure have been described before.<sup>13</sup> We will refer to this specimen preparation technique from here on as the carbon sandwich technique.

The appearance of Tf–TfR complexes prepared by the carbon sandwich technique varied greatly in different areas of the EM grid. In some areas, the particles were still surrounded by stain clouds, suggesting a thin layer of stain accompanied by incomplete stain embedding of the molecules. Occasionally, we found areas where the molecules were embedded in a thick layer of stain, showing fine structure and no stain clouds even at a tilt of 60° (Figure 3(a) and (b)). In other areas the particles appeared larger and showed almost no fine structure, indicating that the molecules became squashed between the two carbon layers upon drying, resulting in massive deformation of the molecules. We used image areas where the particles were mostly unsquashed and did not show stain clouds at a tilt of 60° to collect 60°/0° image pairs. We interactively selected 14,820 pairs of particles. The particles were classified as before, again revealing that the complexes adopt two predominant orientations on the carbon film (Figure 3(c)), but the size of the particles in the class averages varied. The size of the smallest particles (Figure 3(c), panels 1 and 3) corresponded well with that of particles in the class averages of the conventionally stained Tf–TfR complexes (Figure 2(c)). Some class averages showed particles with the same features but a larger size (examples are shown in Figure 3(c), panels 2 and 4). Finally, many class averages showed even larger particles that no longer displayed any discernible structural features of a Tf–TfR complex. An example for an average of such squashed particles is shown in panel 5 of Figure 3(c).

The images that produced the smallest class averages were first used to calculate 3D reconstructions. The unsymmetrized 3D reconstruction (Figure 3(d)) obtained with the particles that produced class average 1 (Figure 3c, panel 1) looks substantially more like the undistorted complex than does the corresponding reconstruction from the Tf–TfR particles prepared by conventional negative staining (Figure 2(d)). All four Tf lobes are represented by densities of almost the same size, and it is not immediately obvious from the 3D map with which side the particle has

adsorbed to the carbon film. The density representing the TfR dimer also shows more fine structure than before and indicates a bipartite organization. The left side of the receptor dimer in the second panel of Figure 3(d) appears, however, to have slid down compared to the right side, obscuring the presence of a 2-fold symmetry in the receptor. After applying the 2-fold symmetry, the density map reveals all the characteristic features of the Tf–TfR complex (Figure 3(e)), including, to some degree, the butterfly shape of the receptor (Figure 3(e), panel 2), but the carbon sandwich technique does not overcome the flattening problem, as the density map is flattened by about 38%.

When we used the top view particles (Figure 3(c), panel 3), the resulting 2-fold symmetrized density map (Figure 3(f)) also looked more like the undistorted complex than the comparable reconstruction from particles prepared by conventional negative staining (Figure 2(f)). As before, these particles suffered more severe flattening (~45%) than the side view particles (~38%), and the features of the Tf–TfR complex were less well resolved. Nevertheless, unlike the reconstruction from particles prepared by conventional negative staining, there is some separation between the densities for TfR and Tf, and there is some indication for the two lobes in the bound Tf molecules.

Finally, we also calculated a 3D reconstruction for one of the classes showing severely deformed Tf–TfR complexes. Like the projection average (Figure 3(c), panel 2), the unsymmetrized 3D reconstruction shows a more extended molecule (Figure 3(g)). In addition, the reconstruction is flatter than the one in Figure 3(d) (6.5 nm instead of 8.5 nm). The Tf lobes appear to be further apart from each other and further removed from the TfR, and the two TfR halves seem to have slid even further apart from each other, removing any indication of dimeric organization (Figure 3(g), panel 2). The whole appearance of this 3D reconstruction is consistent with a “spread-out” Tf–TfR complex, perhaps the result of forces exerted by the two carbon layers that approach each other as the specimen dries.

#### *Cryo-negative staining with uranyl formate using a carbon sandwich and 5% glycerol*

The carbon sandwich technique improved the stain embedding and yielded 3D maps with more fine structure, but the 3D reconstructions still suffered from severe flattening and deformations. To address these remaining problems, we added 5% glycerol to the sample prior to staining with uranyl formate. We then added the second carbon film and froze the sample by plunging it into liquid nitrogen with the glycerol serving to increase the viscosity of the buffer and as cryo-protectant. This preparation technique should conserve the complete stain embedding provided by the carbon sandwich and in addition prevent drying artifacts. The detailed

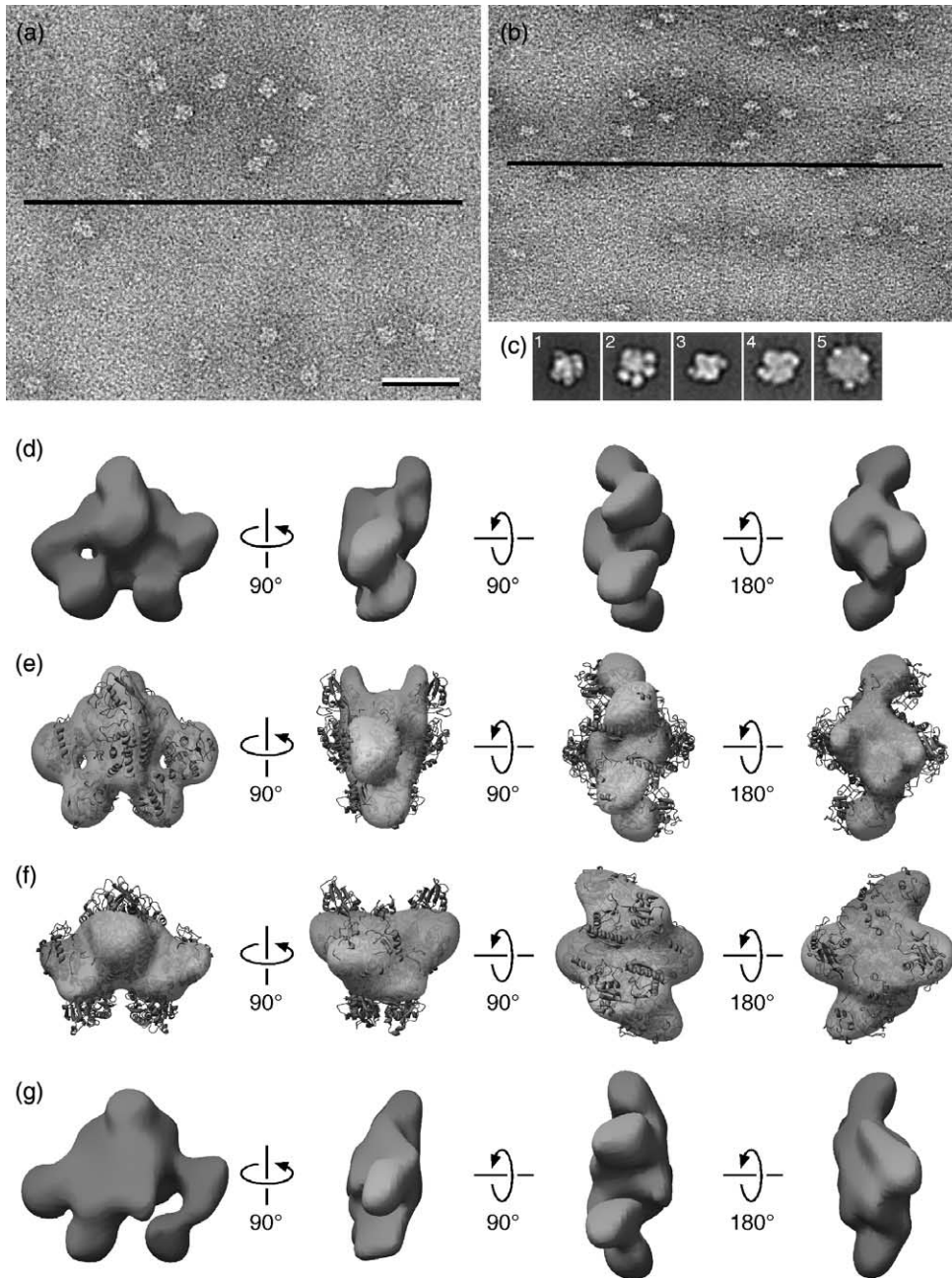


**Figure 3.** Tf-TfR complex prepared by the carbon sandwich technique. (a) and (b) Low-dose images of carbon sandwiched preparations recorded at tilt angles of (a)  $0^\circ$  and (b)  $60^\circ$ . The image of the tilted specimen does not show shadows below the particles, which is characteristic for the conventional negative staining technique. (c) Representative class averages; panel 1, side view; panel 2, side view of flattened particles; panel 3, top view; panel 4, top view of flattened particles; panel 5, average of badly distorted particles showing no recognizable features of a Tf-TfR complex. (d) Views of the unsymmetrized random conical tilt reconstruction obtained with the side view particles (class 1 in (c)). The density representing the receptor is asymmetric and it appears as if the left half of the receptor has slid down with respect to its right half. (e) Same density map as in (d) after 2-fold symmetrization restoring, to some degree, the butterfly shape of the receptor. Fitting of the Tf and TfR crystal structures into the density map reveals that the 3D reconstruction is still flattened. (f) The 2-fold symmetrized 3D reconstruction using the top view particles (class 3 in (c)) revealing substantial flattening, but more structural features than the corresponding reconstruction using complexes prepared by the conventional negative stain technique. (g) Unsymmetrized 3D reconstruction obtained with flattened side view particles (class 2 in (c)) revealing a spread-out morphology of the complex. The scale bar in (a) represents 50 nm and the individual panels in (c) have a side length of 27 nm.

procedure for this sample preparation technique, which we will simply call “cryo-negative staining” (a modified procedure from the one introduced by Stark and co-workers<sup>24</sup> and different from the

technique introduced by Dubochet and co-workers<sup>25</sup>), has been described before.<sup>13</sup>

Cryo-negatively stained samples were imaged at liquid nitrogen temperature. As in the case of

the carbon sandwiched samples, the thickness of the stain layer varied in different areas of the grid, and Tf–TfR complexes in areas with a thin layer of stain showed the typical stain clouds. Tilt pairs (50° and 0°) were thus collected only from areas with a thick layer of stain. Despite strict low-dose procedures, the images often showed white bubbles, particularly in areas with a thick layer of stain. The occurrence of such beam-induced bubbles is a sign of radiation damage and, accordingly, particles in images with bubbles were often of poor quality, having a round shape and no obvious fine structure. We observed the bubbles more frequently in the images of the untilted sample, which were taken after the specimen was already imaged at a 50° tilt. Since particles from images of untilted specimens that showed bubbles aligned poorly to each other, the corresponding particles from the images of the 50° tilted sample could not be used. In the end, only a small percentage of the imaged particles were suitable for calculating 3D reconstructions.

Figure 4(a) and (b) show the two images of a good tilt pair. The particles are embedded in a thick layer of stain, and neither image is visibly affected by radiation damage, so that the image of the untilted sample still shows clear structural features of the Tf–TfR complex (Figure 4(a)). We interactively selected a total of 23,142 particle pairs from 48 image pairs and classified the particles from the images of the untilted sample. Figure 4(c) shows representative class averages. Class averages 1 to 3 show side views of the Tf–TfR complex. The particles represented by average 1 have the expected size and the expected features of the complex, while those represented by average 2 are larger, indicating that they are squashed. Average 3 also represents squashed particles, but in addition this average does not show any fine structure of the complex, indicating that these molecules sustained further damage, possibly related to the radiation-induced bubbles. Class averages 4 and 5 show top views of the Tf–TfR complexes. Average 4 represents particles of the correct size, whereas average 5 contains severely squashed particles. Finally, class average 6 represents molecules that are so badly affected by flattening and beam damage that they no longer show any distinct structural features.

The unsymmetrized 3D reconstruction corresponding to class average 1 shows clear densities for all four Tf lobes and the TfR dimer. The flattening is negligible (Figure 4(d)). Moreover, the second view of the reconstruction shows that the density representing TfR reflects the butterfly shape of the receptor dimer, although it is somewhat deformed. After 2-fold symmetrization, the density map is consistent with the TfR and Tf crystal structures, as seen by their good fit into the map (Figure 4(e)). It is noteworthy that this reconstruction was obtained with only 4190 particles, a sixth of the entire data set. The 3D reconstruction calculated with the top view

particles represented by class average 4 shows significantly less flattening (~34%) (Figure 4(f)) than the corresponding reconstructions from particles prepared by conventional negative staining (Figure 2(f)) or the carbon sandwich technique (Figure 3(f)). The density map shows, however, fewer structural features than the map obtained from carbon sandwiched top view particles (Figure 3(f)). For comparison, we also calculated a 3D reconstruction of a class of larger particles (Figure 4(c), average 2). While the density map (Figure 4(g)) shows the same “spread-out” appearance already seen in the corresponding reconstruction from carbon sandwiched particles (Figure 3(g)), the molecule does not seem to be significantly flattened.

#### *Negative staining with ammonium molybdate in 2% glucose*

A mixture of ammonium molybdate and glucose has previously been used to visualize keyhole limpet hemocyanin type 1, which produced a density map at 15 Å resolution.<sup>26</sup> Glucose embedding is commonly used for preparing two-dimensional crystals,<sup>27,28</sup> but ammonium molybdate has to be added for work on single particles to increase the contrast between the molecules and the embedding medium. The Tf–TfR complex sample was mixed at a 1:1 ratio with a solution of 2% (w/w) glucose and 1% (w/w) ammonium molybdate and applied to a glow-discharged grid before freezing. The mixing of the sample prior to its adsorption to the grid ensured that the Tf–TfR complexes were completely embedded in the stain solution. The images taken from such preparations (Figure 5(a)) show significantly less contrast than those taken from specimens stained with uranyl formate or even those from vitrified specimens (e.g. Figure 1(a)).

A total of 17,107 particles were interactively selected from 39 micrographs and subjected to multiple rounds of MRA and classification using the IMAGIC software package. The resulting class averages revealed that the Tf–TfR complexes assumed many different orientations (Figure 5(b)), similar to complexes embedded in a vitrified ice layer. A 3D reconstruction using the random conical tilt approach was thus impractical. Moreover, despite significant effort, we could not produce a reasonable initial 3D model using the angular reconstitution approach. We therefore used the 2-fold symmetrized 3D reconstruction obtained with vitrified Tf–TfR complex<sup>9</sup> as an initial model, to which we aligned the particle images with FREALIGN. A plot of the Euler angles showed that the particles indeed adopted random and almost uniformly distributed orientations (Figure 5(c)). The Fourier shell correlation (FSC) curve of the final 3D reconstruction using the FSC=0.15 cut-off criterion<sup>29</sup> suggested a resolution of 17 Å (data not shown), better than

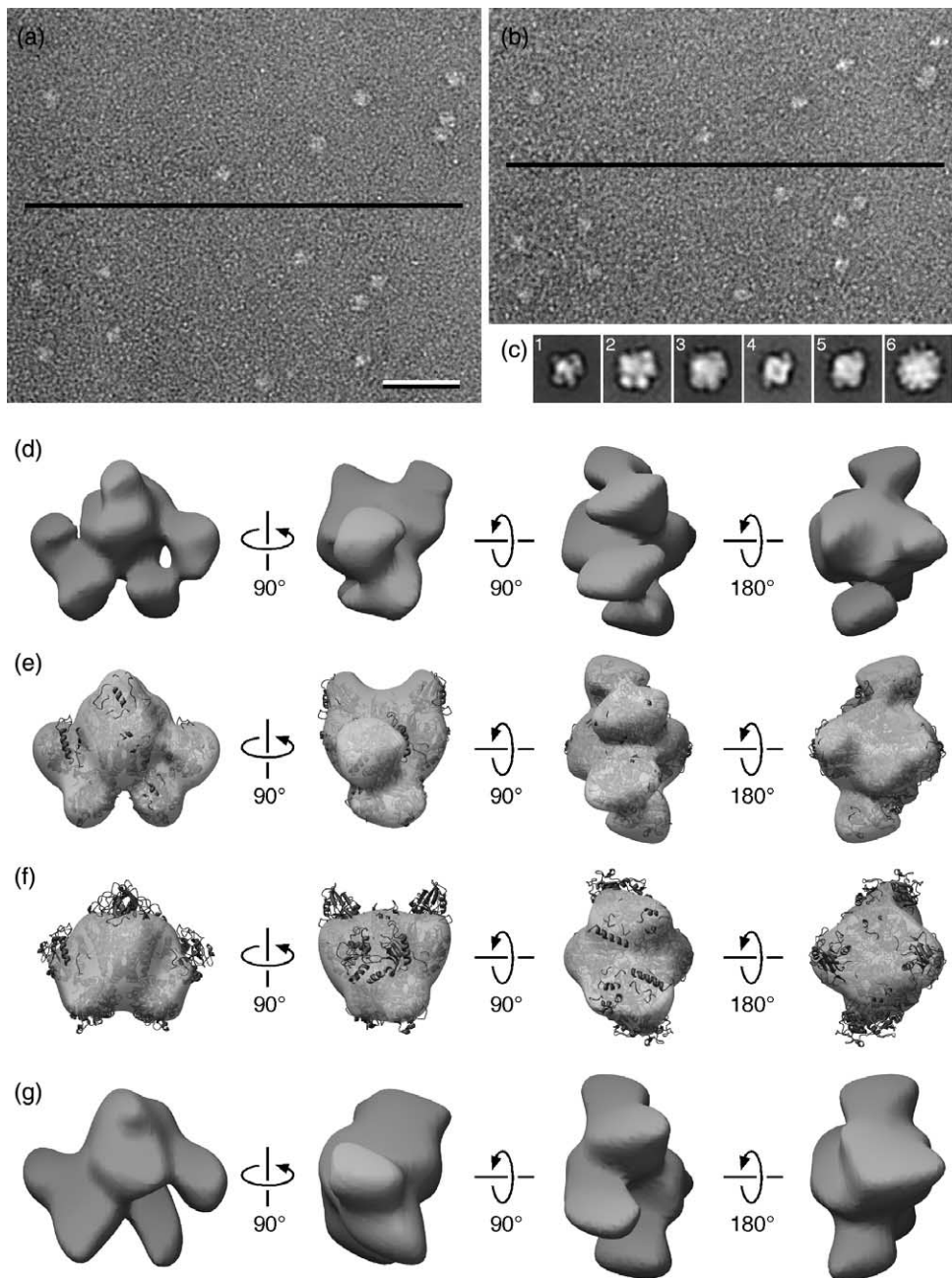


**Figure 4.** Tf-TfR complex prepared by cryo-negative staining. (a) and (b) Low-dose images of cryo-negatively stained specimens recorded at tilt angles of (a)  $0^\circ$  and (b)  $50^\circ$ . (c) Representative class averages; panel 1, side view; panel 2, side view of flattened particles showing clear densities for TfR and Tf; panel 3, side view of flattened particles showing little structural features; panel 4, top view; panel 5, top view of flattened particles; panel 6, average of badly distorted particles showing no recognizable features of a Tf-TfR complex. (d) Views of the unsymmetrized random conical tilt reconstruction obtained with the side view particles (class 1 in (c)). Although the density representing the receptor is somewhat asymmetric, the map shows little flattening. (e) Same density map as in (d) after 2-fold symmetrization with the Tf and TfR crystal structures docked into the density map. The good fit of the crystal structures into the density map indicates that the particles suffered little distortion or flattening. (f) A 2-fold symmetrized 3D reconstruction using the top view particles (class 4 in (c)). Although the density map shows less flattening than the corresponding reconstructions using particles prepared by conventional negative staining and the carbon sandwich technique, the densities representing Tf and TfR are still poorly resolved. (g) Unsymmetrized 3D reconstruction obtained with flattened side view particles (class 2 in (c)). The density map shows a spread-out particle, but little flattening. The scale bar in (a) represents 50 nm and the individual panels in (c) have a side length of 27 nm.

any reconstruction obtained with uranyl formate staining, and the map was filtered to this resolution (Figure 5(d)). While the density map reveals the correct overall shape of the complex

with no major distortions, docking of the TfR and Tf crystal structures showed that the crystal structures protrude from the 3D map in various places.

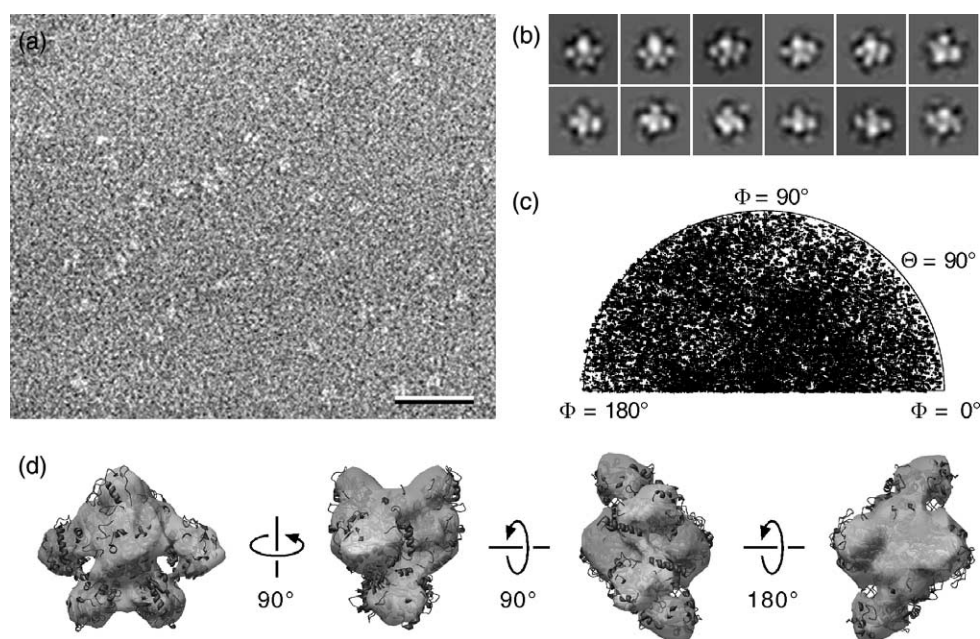


**Figure 5.** Tf-TfR complex prepared with a mixture of ammonium molybdate and glucose. (a) Low-dose image of vitrified Tf-TfR complexes showing the poor image contrast obtained with this preparation technique. (b) Gallery of representative class averages displaying various views of the Tf-TfR complex. (c) Plot of the Euler angle distribution showing that the complex adopts completely random orientations. (d) Views of the 3D reconstruction obtained by using FREALIGN to align the class averages to the 3D map obtained with images of vitrified samples. The scale bar in (a) represents 50 nm and the individual panels in (b) have a side length of 27 nm.

#### Use of FREALIGN to align images of vitrified Tf-TfR complexes to 3D maps obtained by random conical tilt

The 2-fold symmetrized random conical tilt reconstruction obtained with the cryo-negatively stained particles was a very good representation of the structure of the Tf-TfR complex, with virtually no signs of distortion or flattening. We therefore tested whether we could use this map to align the particle images we recorded from the vitrified Tf-TfR complex sample. For this purpose we used FREALIGN,<sup>19</sup> taking full advantage of the 2-fold symmetry of the Tf-TfR complex for both alignment and 3D reconstruction. With FREALIGN we had the choice of either aligning the individual particle images or the class averages to the reference model. Since images taken from vitrified particles are very noisy and have low contrast, we chose to use the class averages whose alignment to the reference model should be less sensitive to spurious features in either the model or the images themselves due to their higher SNR. The individual images of the vitrified Tf-TfR complexes were therefore band-pass filtered to include spatial frequencies between  $1/40 \text{ \AA}^{-1}$  and  $1/170 \text{ \AA}^{-1}$ , including only data before the first node of the CTF, and grouped into 500 classes. The large number of classes was necessary to ensure that the class averages also represented particles adopting less abundant orientations. In FREALIGN, the class averages are aligned directly to the reference model. The Euler angles thus determined were then used to calculate

a new 3D map from the class averages, and this 3D map served, in turn, as a reference model for iterative refinement of the orientational parameters for the class averages. The density map after 15 cycles (Figure 6(b)) was very similar to the 40 Å density map calculated from the atomic model of the complex (Figure 6(a)).

Applying 2-fold symmetry to the 3D reconstruction of the Tf-TfR complex was essential to eliminate distortions in the density map obtained with the cryo-negatively stained sample (compare Figure 4(d) and (e)). We therefore decided to test what would happen in the case of a molecule with no inherent symmetry. Vitrification does not introduce significant distortions in the molecules, whereas cryo-negative staining does. We therefore wondered whether alignment of the class averages from the undistorted vitrified particles would rectify the distortions seen in the reference model obtained from the cryo-negatively stained specimens. Alternatively, it was possible that the distortions of the reference model would impose distortions on the final density map obtained by aligning the class averages from the vitrified particles to the distorted reference model. To simulate an asymmetric molecule, we used as the reference model the density map of cryo-negatively stained Tf-TfR complex produced by random conical tilt without applying 2-fold symmetry (Figure 4(d)). Alignment of the class averages from images of the vitrified complexes and 3D reconstruction using FREALIGN was also performed without enforcing 2-fold symmetry.

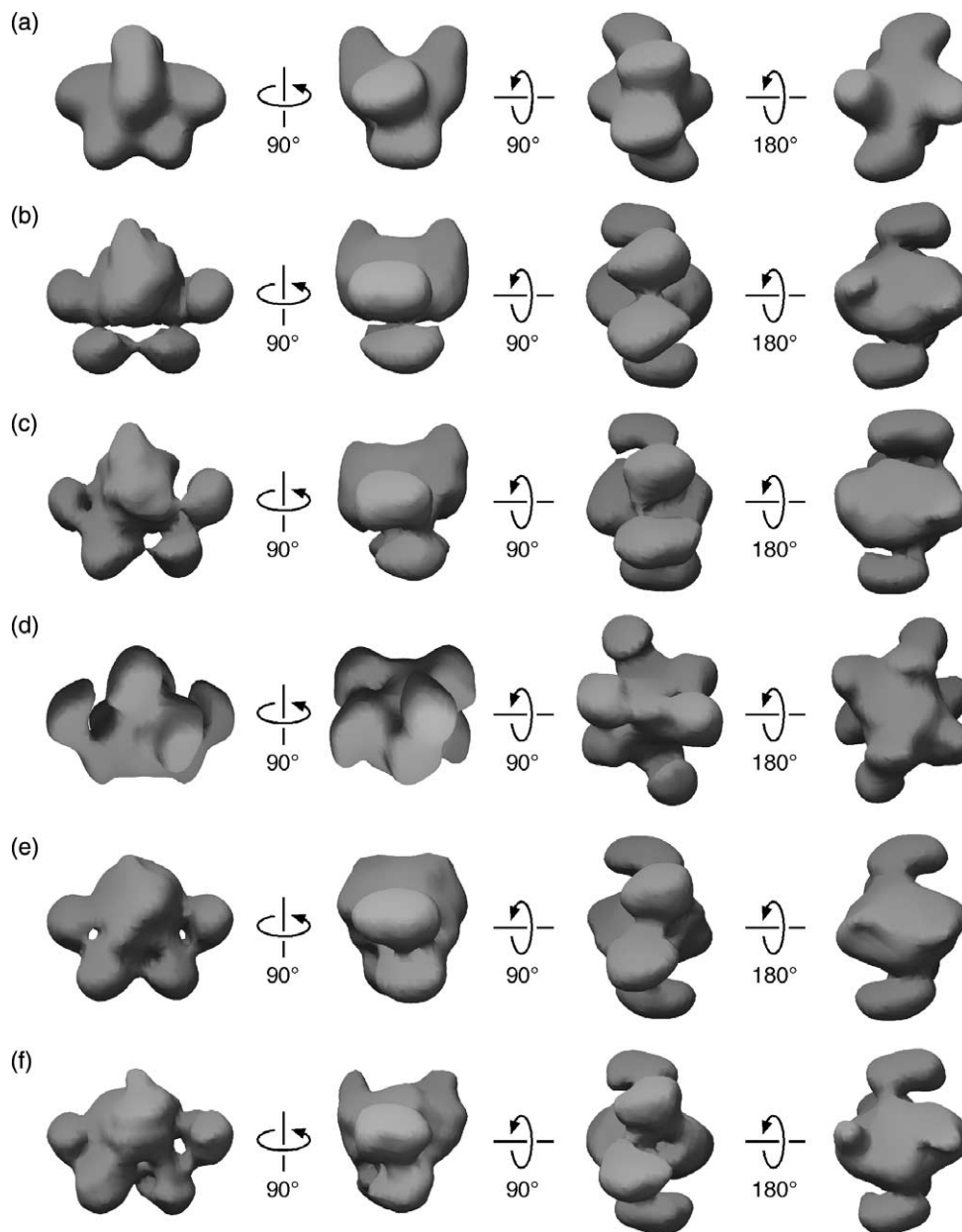


**Figure 6.** Use of random conical tilt reconstructions for the alignment of class averages obtained from images of vitrified particles. (a) Density map obtained by resolution filtering the atomic model of the Tf-TfR complex to 40 Å. (b)–(f) Density maps obtained with FREALIGN. Euler angles were assigned to the class averages calculated from the images of vitrified complexes by directly aligning them to reference maps. The reference maps used were: (b) 2-fold symmetrized 3D reconstruction of the side view particles in cryo-negatively stained preparations; (c) unsymmetrized 3D reconstruction of the side view particles in cryo-negatively stained preparations; (d) 2-fold symmetrized 3D reconstruction of the top view particles in cryo-negatively stained preparations; (e) 2-fold symmetrized 3D reconstruction of the side view particles in samples prepared by conventional negative staining; (f) unsymmetrized 3D reconstruction of the side view particles in samples prepared by conventional negative staining.

The resulting density map showed a reduction of the deformations seen in the 3D reconstruction of the cryo-negatively stained reconstruction, but did not fully restore the 2-fold symmetry of the complex (compare Figure 6(c) with (b)).

We also sought to investigate whether FREALIGN could restore a meaningful density map from the class averages of the vitrified specimen if the reference model was substantially distorted. We first used the 3D reconstruction obtained with

the cryo-negatively stained top view particles, which showed not only substantial flattening but also a lack of distinct structural features (Figure 4(f)). Alignment of the class averages from the vitrified specimen to this reference model resulted in a density map that only slightly resembled the structure of the Tf-TfR complex, even when 2-fold symmetry was enforced (Figure 6(d)). We then used random conical tilt reconstructions obtained from particles negatively

**Table 1.** Comparison of specimen preparation techniques using the Tf-TfR complex

Orientation of particles	Conventional negative staining		Cryo-negative staining	Ammonium molybdate	Vitrified in holes		Vitrified on carbon
	Preferred	Random conical tilt			Carbon sandwich	Preferred	
3D reconstruction approach	Preferred	Random conical tilt	Preferred	Random	Random	Random (slightly preferred <sup>a</sup> )	Random <sup>b</sup>
Specimen flattening	45% (side) 55% (top)	38% (side) 45% (top)	0% (side) 34% (top)	"No flattening" <sup>d</sup>	"No flattening" <sup>d</sup>	No flattening	No flattening
Specimen distortions	Severe distortions	Severe distortions	Minimal distortions	"No distortions" <sup>d</sup>	"No distortions" <sup>d</sup>	No distortions	No distortions
Advantages	High contrast, easy data collection	High contrast, easy data collection	Least flattening, least distortions <sup>d</sup>	"No flattening" <sup>d</sup> "no distortions"	"No flattening" <sup>d</sup> "no distortions"	Perfect specimen preservation	Perfect specimen preservation
Drawbacks	Severe flattening, severe distortions	Severe flattening, severe distortions	Difficult data collection	Not good for random conical tilt <sup>e</sup>	Not good for random conical tilt <sup>e</sup>	Low contrast, not good for random conical tilt <sup>e</sup>	Low contrast, not good for random conical tilt <sup>e</sup>

<sup>a</sup> Particles vitrified on holey carbon films usually adopt random orientations, but some orientation of the particles can occur at the air/water interface.

<sup>b</sup> This result with the Tf-TfR complex is not typical, since vitrification on continuous carbon films usually induces preferred orientations.

<sup>c</sup> Samples with particles in random orientations can also be used for random conical tilt reconstructions, but this requires that very large data sets are collected.

<sup>d</sup> The particles prepared might still be flattened and distorted, but this is not visible in 3D reconstructions calculated by angular reconstitution.

<sup>e</sup> "Not good for random conical tilt" is listed here as a drawback, because of the uncertainties angular reconstitution can introduce in the 3D reconstruction.

stained in the conventional way as reference models. Using the 2-fold symmetrized 3D map of the side view particles (Figure 2(e)) to align the class averages of the vitrified specimen produced a density map in which the flattening of the molecule was no longer obvious (Figure 6(e)). In addition, the density representing the receptor showed a shape much more closely reflecting the true structure of the receptor domain than in the initial model. By contrast, using the 2-fold symmetrized 3D map of the top view particles (Figure 2(f)) as the reference model resulted in a completely uninterpretable map (data not shown). Finally, we used the unsymmetrized side view particle reconstruction from particles negatively stained in the conventional way as reference model (Figure 2(d)) and also did not use the symmetry for the refinement. This imitation of a distorted asymmetric particle produced a density map (Figure 6(f)) that was remarkably similar to the one using the virtually unflattened reference model from the cryo-negative stain preparation (Figure 6(c)).

## Discussion

All the specimen preparation strategies we tested to calculate a single particle 3D reconstruction for the Tf-TfR complex resulted in either an ambiguous density map or a density map affected to varying degrees by preparation artifacts. Our results thus highlight the problem of obtaining a reliable 3D reconstruction by single particle EM with current specimen preparation techniques, drawing attention to the need for careful interpretation of the obtained density maps. While we have used only one test specimen in this study, the Tf-TfR complex is a challenging specimen, and because of its "spiky" structure, it is particularly sensitive to deformations. We therefore believe that many of our findings can be generalized to other specimens, although other specimens may suffer more or less from preparation artifacts depending on their shape and density distribution ("compactness"). What we have learned from our 3D reconstructions is summarized in Table 1 and elaborated in the following paragraphs.

### Influence of the specimen preparation technique on the orientation of the molecules

As expected, vitrified Tf-TfR complexes adopt random, more or less uniformly distributed orientations in holes of holey carbon films (Figure 1(c)). Not expected was our finding that adsorbing the complexes to a continuous carbon film prior to vitrification generated even more randomly distributed orientations (Figure 1(h)). This result shows that adsorption of molecules to a carbon film alone does not guarantee that particles adsorb in preferred orientations. The tendency for preferred orientations of the complexes seen in vitrified samples using holey carbon films may reflect an

alignment of the molecules at the air–water interface, which has been observed before.<sup>30</sup> This notion is somewhat strengthened by our observation that Tf–TfR complexes embedded in a thicker layer of vitrified ice showed a reduced tendency for preferred orientations (data not shown). The more evenly distributed orientations of the molecules adsorbed to a continuous carbon film might therefore be a result of the molecules interacting with the carbon film, keeping them away from the orienting effect of the air–water interface.

Consistent with our experience with all the proteins that we have worked with to date, all negative staining techniques using uranyl formate induced the Tf–TfR complex to adsorb to the carbon support in preferred orientations. In these techniques the specimen was adsorbed to the grid, washed with several drops of water, and then either dried or frozen with or without prior application of a second carbon film. Since in the cryo-negative staining procedure the grid is frozen before it is completely dry, complete drying of the grid cannot be the only reason leading to preferred orientations of the molecules. Instead, it is likely that the washing steps remove the majority of particles that are only lightly attached to the carbon film, leaving behind only particles that have a substantial interaction surface with the carbon layer. Images taken from specimens stained with ammonium molybdate showed molecules in random and uniformly distributed orientations (Figure 5(c)). In this case the sample was pre-mixed with the glucose-containing staining solution, and the grid was not washed after application of the sample.

The orientations in which a molecule will adsorb to a grid will always depend on the chemical and morphological characteristics of the molecule itself, but based on our experiments we can identify factors that influence the adsorption behavior of molecules. Our observations suggest that for molecules adsorbed to a carbon film, washing steps and complete drying of the grid are factors that tend to favor preferred orientations, whereas pre-mixing the sample with a stain/sugar solution and freezing of the grid are factors that tend to favor random orientations.

### Flattening and distortions introduced by the specimen preparation technique

The density map produced by random conical tilt using side view particles of Tf–TfR complex prepared by the conventional negative staining technique suffers from substantial preparation-induced artifacts. One side of the unsymmetrized reconstruction is flat (Figure 2(d), left side in views 2 to 4). Also, in one of the Tf molecules the two lobes are closer together, and in this Tf molecule the Tf C-lobe is notably smaller than in the other Tf molecule (marked by an asterisk in views 1 and 4 of Figure 2(d)). In addition, the density representing the TfR dimer shows no indication of its characteristic butterfly shape. Finally, the reconstruction is severely flattened.

Such deformations induced by negative staining are well known and have already been analyzed by a number of investigators.<sup>31,32</sup>

A flat surface on one side of the reconstruction is seen in the reconstruction from negatively stained particles and, to a lesser degree, in the unsymmetrized reconstructions from both the carbon sandwiched (Figure 3(d)) and the cryo-negatively stained particles (Figure 4(d)). The flat surface most likely represents the interface of the complex with the carbon layer. This distortion can probably not be avoided, but it is minimal in samples prepared by cryo-negative staining. The two Tfs are bound to the TfR dimer off-axis, so that when the complex adsorbs to the carbon film, one of the Tfs will come into contact with the carbon film more extensively than the other one. This is most likely the reason for the observed asymmetry between the two Tf molecules, as the Tf making more contact with the carbon film is likely to be more deformed than the other Tf. Indeed, the Tf molecule with the more closely spaced lobes and the small C-lobe is close to the flattened surface of the reconstruction (Figure 2(d), view 4). Similar distortions can also be seen in the unsymmetrized reconstructions from carbon sandwiched (Figure 3(d)) and cryo-negatively stained particles (Figure 4(d)), but the effect is more subtle and the C-lobe of the Tf molecule close to the carbon film does not appear significantly smaller than that of the other Tf.

The density representing the TfR shows the strongest deformations when prepared by the conventional negative staining protocol and completely lacks any indication of a bipartite organization or the characteristic butterfly shape of the receptor dimer (Figure 2(d), view 2). There are several possible explanations for the lack of structural detail in the TfR density, such as the missing cone problem, structural collapse of the receptor upon drying of the grid, and incomplete embedding of the receptor in the stain layer. The missing cone problem results from the fact that specimens can only be tilted to a limited angle in the electron microscope, typically not more than 60°, which prevents the sampling of a cone-shaped volume in Fourier space. This leads to an anisotropic resolution of the reconstructed density map with the resolution in the direction perpendicular to the carbon film being lower than the in-plane resolution. Both the unsymmetrized maps from carbon sandwiched (Figure 3(d)) and cryo-negatively stained particles (Figure 4(d)) were reconstructed from data collected in the same way as the data for the particles negatively stained by the conventional method. These density maps show clear indications for both TfRs in the dimer. We therefore exclude the missing cone as the cause for the loss of structural detail in the density representing the TfR dimer. The lack of structural detail probably results from the combined effect of incomplete stain embedding and structural collapse. In particles adsorbed to the carbon presenting the side view, the TfR constitutes the

density furthest removed from the carbon support. It is therefore conceivable that the TfR in the dimer further removed from the carbon film protrudes from the stain layer and is thus “invisible”. In addition, the apical domains, which represent the tips of the butterfly wings, are only loosely attached to the remainder of the TfR molecules and therefore may easily be displaced.<sup>22</sup> It is quite likely that the apical domain of the TfR molecule further away from the carbon film collapses on top of the apical domain of the TfR in contact with the carbon film. Although the unsymmetrized density maps calculated from carbon sandwiched (Figure 3(d)) and cryo-negatively stained particles (Figure 4(d)) show more of the butterfly shape of the receptor dimer, they also reveal distortions. In the reconstruction from the carbon sandwiched molecules, the receptor in contact with the carbon film (left side in view 2 of Figure 3(d)) seems to have slid down relative to the TfR not in contact with the carbon. The distortions seen in the density maps calculated from the carbon sandwiched and cryo-negatively stained particles thus may again represent effects of the adsorption of the molecules to a carbon film.

The use of a second carbon film covering the sample clearly has a beneficial effect on the outcome of the 3D reconstruction (compare Figure 3(d) with Figure 2(d)). This is most likely caused by a better embedding of the particles in the stain layer, which is the reason why the carbon sandwich technique was originally introduced.<sup>23</sup> The complete stain embedding is reflected by the lack of a stain shadow below the particles in images of tilted specimens, which is advantageous, because the strong contrast between the stain and the particle may influence the alignment of the particle images. Since this strong feature depends solely on the orientation of the tilt axis rather than on the inherent structure of the molecules, the stain cloud could interfere with the alignment of the particles according to their less strongly contrasted inherent features.

The distance between the two carbon films sandwiching the particles is crucial. Too big a distance results in a thick stain layer, in which the particles are difficult to see, whereas too small a distance leads to squashing of the particles. This squashing is different from the simple flattening of molecules upon drying of the specimen, since the former leads to projection averages that show the particles to be enlarged, whereas the latter has only little influence on the appearance of the particles in projection averages: 3D reconstructions of squashed particles are shown in Figures 3(g) and 4(g), which show a spread-out appearance of the molecule. The density map of the squashed molecules from the images of carbon sandwiched preparations (Figure 3(g), view 2) is also slightly more flattened than that of the unsquashed particle (Figure 3(d), view 2). This is consistent with the two approaching carbon films exerting force on the trapped molecules. The density map of the squashed molecules obtained with the cryo-negatively stained particles does not, however, show such an

increased flattening (Figure 4(g), view 2) compared to the unsquashed particle (Figure 4(d), view 2). This comparison indicates that the squashing of the particles by the two carbon layers does not simply reflect mechanical force experienced by the sandwiched particles.

Symmetry as low as 2-fold in the imaged molecule can substantially improve the density map. Many distortions seen in the unsymmetrized maps of the side view particles (Figures 2(d), 3(d), and 4(d)) were corrected, at least to some degree, by applying the 2-fold symmetry of the Tf–TfR complex to the density map (Figures 2(e), 3(e), and 4(e)). 2-fold symmetrization does not, however, correct for the substantial flattening seen in the reconstructions from the top view particles (Figures 2(f), 3(f), and 4(f)), which do not look significantly different from the unsymmetrized reconstructions (data not shown). The reconstructions from the top view particles thus make the point that application of symmetry to single particle reconstructions is only helpful in reducing distortion artifacts if the molecule does not adsorb to the carbon support film with its symmetry axis oriented perpendicular to the carbon film.

Staining with an ammonium molybdate/glucose mixture produced images with low contrast (Figure 5(a)), and the particles were adsorbed to the carbon film in random orientations (Figure 5(c)). Because of the poor SNR of the images, the class averages (Figure 5(b)) also appeared noisier than those obtained from images of vitrified samples (Figure 1(b)). This might be the reason why we failed with this data set to produce a reasonable initial 3D map with the angular reconstitution approach and had to align the class averages to the density map obtained with the images of the vitrified specimen. The final 3D map shows few distortions (Figure 5(d)). Absence of distortions does not mean, however, that the particles are unflattened. As seen, for example, in the projection averages from the conventionally negatively stained particles (Figure 2(c)), flattening due to specimen drying does not show up in projections. Since we had uniformly distributed views of the particles, and therefore could not calculate a random conical tilt 3D reconstruction, we cannot judge the extent of flattening introduced by this specimen preparation technique. Since the images showed less contrast than those of uranyl formate stained specimens (ideal for random conical tilt) or even vitrified specimens (ideal for angular reconstitution), we do not view staining with a glucose-containing ammonium molybdate solution as an advantageous specimen preparation technique.

Cryo-negative staining appears to produce the best 3D reconstructions displaying the least distortions and flattening artifacts, especially if symmetry can be applied to the density map as in the case of the Tf–TfR complex. Preparation and imaging of cryo-negatively stained samples is not straightforward, however. Often grids prepared in this way show the particles to be positively stained, making these grids useless for

data collection. In addition, different areas of the grid can vary greatly, showing areas with stain layers too thin or too thick. Even in areas that appear to have a stain layer of optimal thickness, many particles are squashed and are thus unsuitable for 3D reconstruction. Moreover, cryo-negatively stained samples are particularly radiation sensitive, so that many images show beam-induced bubbles. All these effects combined account for a very low yield of good particles that can be used for 3D reconstruction. We think that the improved quality of the resulting density maps compensates for the increased amount of work needed to assemble a large enough data set. We note, however, that even with the cryo-negative staining procedure, reliable density maps are only obtained in favorable cases. Under unfavorable conditions, particles prepared by this technique can produce badly distorted and flattened reconstructions as illustrated by the density map obtained with the top view particles (Figure 4(f)).

### Influence of the reference model on the final reconstruction

We believe that the most reliable initial 3D density map would be obtained by calculating a random conical tilt reconstruction using tilt pairs taken from vitrified specimens. This approach combines the advantage of specimen vitrification, i.e. few preparation artifacts, with the reliability of the random conical tilt 3D reconstruction technique. In some favorable cases this approach is feasible, such as with molecules that are large enough and adopt preferred orientations in the vitreous ice layer, as in the case of the ryanodine receptor.<sup>32</sup> Collecting tilt pairs of vitrified specimens is extremely difficult, however, and for the ryanodine receptor only nine out of several hundred image pairs were of sufficiently high quality to be useful for image processing.<sup>32</sup> Despite this technical challenge we attempted to record tilt pairs of the vitrified Tf-TfR complex, but the small size of the complex made it almost impossible to see the molecules in images taken from tilted specimen and to correlate them to the corresponding particles in the images of the untilted specimen.

We therefore tested whether random conical tilt reconstructions obtained with specimens prepared by various negative staining techniques could be used as models to guide the 3D reconstruction using images taken from vitrified specimens. We chose to align class averages rather than raw images to the reference models, because of their better SNRs. Furthermore, to make the results independent of CTF effects, we low pass-filtered the raw images to a resolution of 40 Å before calculating the class averages that were used for the alignment to the reference models. We did not refine the resulting density maps to high resolution, because our main interest here was the overall shape of the density maps and, in particular, how the shape of the

density map was influenced by that of the reference model.

We first used our best random conical tilt 3D reconstruction, the 2-fold symmetrized density map obtained with the cryo-negatively stained side view particles (Figure 4(e)), and FREALIGN produced a density map with a very accurate shape (Figure 6(b)). To simulate an asymmetric molecule, we used the unsymmetrized density map obtained with the cryo-negatively stained side view particles (Figure 4(d)) as reference model and abstained from using the 2-fold symmetry in the refinement process. The resulting density map did not show a perfect 2-fold symmetry (Figure 6(c)), but the density map was clearly improved over the reference model. This result strongly suggests that the refinement procedure can, at least to some degree, overcome distortions present in the reference model. This was not the case, however, when we used the 2-fold symmetrized density map obtained with the cryo-negatively stained top view particles as reference model, even when 2-fold symmetry was enforced during the refinement (Figure 4(f)). In this case, the resulting density map looked only very remotely similar to the structure of the Tf-TfR complex (Figure 6(d)). The unrecognizable density map is most likely due to misalignment of many class averages to the almost featureless reference map. When we used the 2-fold symmetrized density map obtained with the conventionally negatively stained top view particles as reference model, we produced a similarly unrecognizable reconstruction (data not shown). A density map resulting from refinement with FREALIGN that looks very different from the initial reference map may thus indicate that the initial model was inaccurate, e.g. because it suffered from substantial distortions and flattening artifacts. Further studies are then needed to determine whether the “refined” density map is indeed a good representation of the true structure of the molecule. Finally, we used the unsymmetrized and 2-fold symmetrized density maps obtained with the conventionally negatively stained side view particles (Figure 2(d) and (e)) and performed the refinement without and with enforced 2-fold symmetry, respectively. Both refinements produced a density map (Figure 6(e) and (f)) that was significantly improved over the respective reference model in terms of flattening and asymmetry. These results indicate that even a significantly flattened reference model can be used to align the class images from vitrified specimens, as long as it shows a sufficient amount of correct structural detail to warrant successful matching of the averages to the reference model.

### Conclusions

Our results show that 3D reconstructions obtained by single particle EM are often far from perfect. This finding emphasizes the need for very

Careful analysis of the density maps produced by this technique, especially if molecules with unknown structures are studied. The angular reconstitution approach, commonly used to analyze images of vitrified specimens, can potentially produce inaccurate reconstructions, although a high symmetry of the molecule under investigation usually overcomes this caveat. In the case of molecules with low or no inherent symmetry, 3D maps obtained with the angular reconstitution approach should be viewed with great skepticism and not be trusted blindly unless confirmed by other structural information, such as crystal structures or independently determined 3D reconstructions. The random conical tilt approach produces unambiguous reconstructions. Since this approach requires the molecules to adopt preferred orientations, which is often only seen in negatively stained specimens, the density maps are often affected by distortions and flattening artifacts due to the need to adsorb the molecules to a carbon film and to dry the specimen. Even in the most sophisticated negative staining procedures, such as cryo-negative staining, distortions cannot be ruled out. Although the distortions cannot be predicted, they can be understood, as they primarily affect features of the molecule perpendicular to the carbon film. Random conical tilt reconstructions of negatively stained specimens can therefore be used to validate or discount density maps obtained by angular reconstitution of vitrified specimens. Alternatively, a random conical tilt reconstruction obtained with a cryo-negatively stained specimen can be used as reference model to align images taken from vitrified specimens. The program FREALIGN is fast and well suited for this purpose. While the reference model can introduce subtle artifacts in the final reconstruction obtained with the ice data, distortions and flattening artifacts of the reference model are largely removed during the refinement process. This procedure fails, however, if the reference model is substantially distorted. A large difference between the reference model and the final map is thus an indication that the chosen reference model may not have been a good representation of the molecular structure.

## Materials and Methods

### Specimen preparation and electron microscopy

Recombinant human Tf-TfR complex was prepared as described<sup>9</sup> and diluted to a concentration of about 0.01 mg/ml. Vitrification of Tf-TfR complex was done as described.<sup>9</sup> Protocols for conventional negative staining, the carbon sandwich technique, ammonium molybdate staining, and cryo-negative staining have been described.<sup>13</sup> Images of vitrified specimens were recorded with a Tecnai F20 electron microscope as described.<sup>9</sup>

Specimens prepared by conventional negative staining and the carbon sandwich technique were imaged at room temperature in a Gatan 670 ultra-high tilt holder, whereas specimens prepared by ammonium molybdate and

cryo-negative staining were imaged at liquid nitrogen temperature of about  $-180^{\circ}\text{C}$  in an Oxford cryo-transfer holder. Samples prepared with ammonium molybdate were imaged at  $0^{\circ}$  tilt, while samples prepared by conventional negative staining and the carbon sandwich technique were imaged at tilt angles of  $60^{\circ}$  and  $0^{\circ}$ . In the case of cryo-negative staining the sample was imaged at tilt angles of  $50^{\circ}$  and  $0^{\circ}$ . All images were taken with an FEI Tecnai T12 microscope equipped with an LaB<sub>6</sub> filament and operated at 120 kV. Images were taken at a magnification of  $52,000\times$  on Kodak SO-163 film using low-dose procedures and developed for 12 min with full-strength Kodak D-19 developer at  $20^{\circ}\text{C}$ . All micrographs were visually inspected with an optical laser diffractometer and only drift-free images were digitized with a Zeiss SCAI scanner using a step size of  $7\ \mu\text{m}$ . The digitized images were further averaged over  $3\times 3$  pixels to give a final pixel size of  $4.04\ \text{\AA}/\text{pixel}$  at the specimen level.

### Image processing

Images of vitrified Tf-TfR complex prepared with holey carbon film were processed as described.<sup>9</sup> Briefly, a total of 36,266 particles were selected interactively from 196 micrographs using Ximdisp, the display program associated with the MRC program suite.<sup>33</sup> Using the IMAGIC software package<sup>16</sup> the windowed particles were band-pass filtered to a resolution of  $170\ \text{\AA}$  to  $40\ \text{\AA}$ , followed by five cycles of MRA, MSA and classification into 500 classes. A total of 124 class averages were selected out of the final 500 class averages. Euler angles were assigned to these class averages using the Angular Reconstitution command in IMAGIC with the NEW\_PROJECTION/FRESH option. The class averages with the assigned Euler angles were then used to calculate a 3D reconstruction. Projections calculated from the 3D reconstruction at an angular interval of  $15^{\circ}$  were used as anchor set to further refine the Euler angles of the class averages. After two cycles of Euler angle refinement using anchor sets, 157 additional class averages were added into the data set. A total of six cycles of Euler angle refinement was performed and the final 3D reconstruction shown in Figure 1(d) calculated from a total of 281 class averages.

Images of vitrified Tf-TfR complex adsorbed to continuous carbon film were recorded and digitized in the same way as for the vitrified Tf-TfR complex on holey carbon film. A total of 21,719 particles were selected interactively from 46 micrographs. The particles were band-pass filtered as before, followed by only one cycle of MRA, MSA and classification into 500 classes. The refined model of the Tf-TfR complex<sup>9</sup> was filtered to  $10\ \text{\AA}$  and used to calculate projections at an angular interval of  $15^{\circ}$ . These projections were used as anchor set to assign Euler angles to all 500 class averages. The resulting 3D map was used as reference model to which the raw particle images were aligned with FREALIGN. The density map was refined to  $7.5\ \text{\AA}$ .

For images of the Tf-TfR complex stained with ammonium molybdate, a total of 17,107 particles were interactively selected from 39 micrographs. The particles were band-pass filtered and subjected to five cycles of MRA, MSA and classification. As for the vitrified Tf-TfR complex on continuous carbon film, the Euler angles of the final 500 class averages were determined using the anchor set created from the refined 3D model of the vitrified Tf-TfR complex on holey carbon film, and further refined with FREALIGN.

All tilt pairs were processed using the SPIDER software package.<sup>17</sup> Particles were selected interactively using

WEB, the display program associated with SPIDER. The particles from the images of the untilted specimens were subjected to eight cycles of multi-reference alignment and classification into 50 classes. Class averages showing the same projection structure were combined for further processing. The initial 3D reconstructions were calculated with the particles selected from the images of the tilted specimens using the random conical approach.<sup>10</sup> 10% of the particles from the corresponding classes from the images of the untilted specimens were then added to the data set and the structures refined by ten cycles of angular refinement, which is based on projection matching. The final resolutions of the 3D reconstructions were estimated from the Fourier shell correlation (FSC) curve using the FSC=0.5 cut-off criterion.

For the Tf-TfR complex prepared by the conventional negative staining procedure, a total of 8410 pairs of particles were selected from 84 pairs of micrographs. The reconstructions shown in Figure 2 contain 1461 particles (Figure 2(d) and (e)) and 1412 particles (Figure 2(f)). The resolutions for the 3D reconstructions shown in Figure 2(e) and (f) were determined as 27 Å.

For the Tf-TfR complex prepared by the carbon sandwich technique, a total of 14,820 pairs of particles were selected from 54 pairs of micrographs. The reconstructions shown in Figure 3 contain 5163 particles (Figure 3(d) and (e)), 468 particles (Figure 3(f)), and 512 particles (Figure 3(g)). The resolutions for the 3D reconstructions shown in Figure 3(e), (f), and (g) were determined as 22 Å, 30 Å, and 27 Å.

For the Tf-TfR complex prepared by cryo-negative staining, a total of 23,142 pairs of particles were selected from 48 pairs of micrographs. The reconstructions shown in Figure 4 contain 4190 particles (Figure 4(d) and (e)), 380 particles (Figure 4(f)), and 424 particles (Figure 4(g)). The resolutions for the 3D reconstructions shown in Figure 4(e), (f), and (g) were determined as 24 Å, 29 Å, and 29 Å.

FREALIGN was used to assign Euler angles to the 500 class averages of the vitrified Tf-TfR complex. The 3D reconstructions obtained with the random conical tilt approach were used as initial reference models. Option 3 in FREALIGN (simple search and refine) was used with a 15° angular step size and a refinement limitation of 20 Å.

Docking of the atomic structure of the Tf-TfR complex (pdb code: 1SUV) into the density maps was done manually using the program Chimera.<sup>34</sup>

## Acknowledgements

We thank Pawel Penczek for many valuable suggestions. This work was supported by National Institutes of Health Grant GM62580 (to David DeRosier). The molecular EM facility at Harvard Medical School was established by a generous donation from the Giovanni Armenise Harvard Center for Structural Biology.

## References

- Bottcher, B., Wynne, S. A. & Crowther, R. A. (1997). Determination of the fold of the core protein of hepatitis B virus by electron cryomicroscopy. *Nature*, **386**, 88–91.
- Zhou, Z. H., Dougherty, M., Jakana, J., He, J., Rixon, F. J. & Chiu, W. (2000). Seeing the herpesvirus capsid at 8.5 Å. *Science*, **288**, 877–880.
- Gabashvili, I. S., Agrawal, R. K., Spahn, C. M., Grassucci, R. A., Svergun, D. I., Frank, J. & Penczek, P. (2000). Solution structure of the *E. coli* 70S ribosome at 11.5 Å resolution. *Cell*, **100**, 537–549.
- Stark, H., Rodnina, M. V., Wieden, H. J., van Heel, M. & Wintermeyer, W. (2000). Large-scale movement of elongation factor G and extensive conformational change of the ribosome during translocation. *Cell*, **100**, 301–309.
- Jurica, M. S., Sousa, D., Moore, M. J. & Grigorieff, N. (2004). Three-dimensional structure of C complex spliceosomes by electron microscopy. *Nature Struct. Mol. Biol.* **11**, 265–269.
- Boehringer, D., Makarov, E. M., Sander, B., Makarova, O. V., Kastner, B., Luhrmann, R. & Stark, H. (2004). Three-dimensional structure of a pre-catalytic human spliceosomal complex B. *Nature Struct. Mol. Biol.* **11**, 463–468.
- Stark, H., Dube, P., Luhrmann, R. & Kastner, B. (2001). Arrangement of RNA and proteins in the spliceosomal U1 small nuclear ribonucleoprotein particle. *Nature*, **409**, 539–542.
- Orlova, E. V., Rahman, M. A., Gowen, B., Volynski, K. E., Ashton, A. C., Manser, C. *et al.* (2000). Structure of alpha-latrotoxin oligomers reveals that divalent cation-dependent tetramers form membrane pores. *Nature Struct. Biol.* **7**, 48–53.
- Cheng, Y., Zak, O., Aisen, P., Harrison, S. C. & Walz, T. (2004). Structure of the human transferrin receptor-transferrin complex. *Cell*, **116**, 565–576.
- Radermacher, M., Wagenknecht, T., Verschoor, A. & Frank, J. (1987). Three-dimensional reconstruction from a single-exposure, random conical tilt series applied to the 50 S ribosomal subunit of *Escherichia coli*. *J. Microsc.* **146**, 113–136.
- van Heel, M. (1987). Angular reconstitution: a posteriori assignment of projection directions for 3D reconstruction. *Ultramicroscopy*, **21**, 111–123.
- Bremer, A., Henn, C., Engel, A., Baumeister, W. & Aebi, U. (1992). Has negative staining still a place in biomacromolecular electron microscopy? *Ultramicroscopy*, **46**, 85–111.
- Ohi, M., Li, Y., Cheng, Y. & Walz, T. (2004). Negative staining and image classification—powerful tools in modern electron microscopy. *Biol. Proc. Online*, **6**, 23–34.
- Adrian, M., Dubochet, J., Lepault, J. & McDowell, A. W. (1984). Cryo-electron microscopy of viruses. *Nature*, **308**, 32–36.
- van Heel, M., Winkler, H. P., Orlova, E. V. & Schatz, M. (1992). Structural analysis of ice-embedded single particles. *Scanning Microsc. Suppl.* **6**, 23–42.
- van Heel, M., Harauz, G., Orlova, E. V., Schmidt, R. & Schatz, M. (1996). A new generation of the IMAGIC image processing system. *J. Struct. Biol.* **116**, 17–24.
- Frank, J., Rademacher, M., Penczek, P., Zhu, J., Ladjadj, M. & Leith, A. (1996). SPIDER and WEB: processing and visualization of images in 3D electron microscopy and related fields. *J. Struct. Biol.* **116**, 190–199.
- Ludtke, S. J., Baldwin, P. R. & Chiu, W. (1999). EMAN: semiautomated software for high-resolution single-particle reconstructions. *J. Struct. Biol.* **128**, 82–97.
- Stewart, A. & Grigorieff, N. (2004). Noise bias in the refinement of structures derived from single particles. *Ultramicroscopy*, **102**, 67–84.

20. Penczek, P. A., Zhu, J. & Frank, J. (1996). A common-lines based method for determining orientations for  $N > 3$  particle projections simultaneously. *Ultramicroscopy*, **63**, 205–218.
21. Hall, D. R., Hadden, J. M., Leonard, G. A., Bailey, S., Neu, M., Winn, M. & Lindley, P. F. (2002). The crystal and molecular structures of diferric porcine and rabbit serum transferrins at resolutions of 2.15 and 2.60 Å, respectively. *Acta Crystallog. sect. D*, **58**, 70–80.
22. Lawrence, C. M., Ray, S., Babyonyshev, M., Galluser, R., Borhani, D. W. & Harrison, S. C. (1999). Crystal structure of the ectodomain of human transferrin receptor. *Science*, **286**, 779–782.
23. Stoffler-Meilicke, M. & Stoffler, G. (1988). Localization of ribosomal proteins on the surface of ribosomal subunits from *Escherichia coli* using immunoelectron microscopy. *Methods Enzymol.* **164**, 503–520.
24. Golas, M. M., Sander, B., Will, C. L., Luhrmann, R. & Stark, H. (2003). Molecular architecture of the multi-protein splicing factor SF3b. *Science*, **300**, 980–984.
25. Adrian, M., Dubochet, J., Fuller, S. D. & Harris, J. R. (1998). Cryo-negative staining. *Micron*, **29**, 145–160.
26. Orlova, E. V., Dube, P., Harris, J. R., Beckman, E., Zemlin, F., Markl, J. & van Heel, M. (1997). Structure of keyhole limpet hemocyanin type 1 (KLH1) at 15 Å resolution by electron cryomicroscopy and angular reconstitution. *J. Mol. Biol.* **271**, 417–437.
27. Unwin, P. N. & Henderson, R. (1975). Molecular structure determination by electron microscopy of unstained crystalline specimens. *J. Mol. Biol.* **94**, 425–440.
28. Gonen, T., Sliz, P., Kistler, J., Cheng, Y. & Walz, T. (2004). Aquaporin-0 membrane junctions reveal the structure of a closed water pore. *Nature*, **429**, 193–197.
29. Rosenthal, P. B. & Henderson, R. (2003). Optimal determination of particle orientation, absolute hand, and contrast loss in single-particle electron cryomicroscopy. *J. Mol. Biol.* **333**, 721–745.
30. Grigorieff, N. (1998). Three-dimensional structure of bovine NADH:ubiquinone oxidoreductase (complex I) at 22 Å in ice. *J. Mol. Biol.* **277**, 1033–1046.
31. Boisset, N., Taveau, J. C., Lamy, J., Wagenknecht, T., Radermacher, M. & Frank, J. (1990). Three-dimensional reconstruction of native *Androctonus australis* hemocyanin. *J. Mol. Biol.* **216**, 743–760.
32. Radermacher, M., Rao, V., Grassucci, R., Frank, J., Timerman, A. P., Fleischer, S. & Wagenknecht, T. (1994). Cryo-electron microscopy and three-dimensional reconstruction of the calcium release channel/ryanodine receptor from skeletal muscle. *J. Cell. Biol.* **127**, 411–423.
33. Crowther, R. A., Henderson, R. & Smith, J. M. (1996). MRC image processing programs. *J. Struct. Biol.* **116**, 9–16.
34. Pettersen, E. F., Goddard, T. D., Huang, C. C., Couch, G. S., Greenblatt, D. M., Meng, E. C. & Ferrin, T. E. (2004). UCSF Chimera—a visualization system for exploratory research and analysis. *J. Comput. Chem.* **25**, 1605–1612.

*Edited by W. Baumeister*

(Received 3 October 2005; received in revised form 31 October 2005; accepted 7 November 2005)  
Available online 28 November 2005